Towards Quantification of Myelin by Solid-State MRI of the Lipid Matrix Protons

Alan C. Seifert[1,4,†], **Cheng Li**[1,†], **Michael J. Wilhelm**[2], **Suzanne L. Wehrli**[3], and **Felix W. Wehrli**[1,*]

[1]Laboratory for Structural, Physiologic and Functional Imaging, Department of Radiology, Perelman School of Medicine, University of Pennsylvania, 1 Founders Pavilion, 3400 Spruce Street, Philadelphia, PA 19104 USA

[2]Department of Chemistry, Temple University, 1901 N. 13th St., Philadelphia, PA 19122 USA

[3]SAIF Core Facility, The Children's Hospital of Philadelphia, Room 413 Abramson Building, 34th Street and Civic Center Boulevard, Philadelphia, PA 19104 USA

Abstract

Purpose—Direct assessment of myelin has the potential to reveal central nervous system abnormalities and serve as a means to follow patients with demyelinating disorders during treatment. Here, we investigated the feasibility of direct imaging and quantification of the myelin proton pool, without the many possible confounds inherent to indirect methods, via long-T_2 suppressed 3D ultra-short echo-time (UTE) and zero echo-time (ZTE) MRI in ovine spinal cord.

Methods—ZTE and UTE experiments, with and without inversion-recovery (IR) preparation, were conducted in ovine spinal cords before and after D_2O exchange of tissue water, on a 9.4T vertical-bore micro-imaging system, along with some feasibility experiments on a 3T whole-body scanner. Myelin density was quantified relative to reference samples containing various mass fractions of purified myelin lipid, extracted via the sucrose gradient extraction technique, and reconstituted by suspension in water, where they spontaneously self-assemble into an ensemble of multi-lamellar liposomes, analogous to native myelin.

Results—MR signal amplitudes from reference samples at 9.4T were linearly correlated with myelin concentration (R^2 = 0.98–0.99), enabling their use in quantification of myelin fraction in neural tissues. An adiabatic inversion-recovery preparation was found to effectively suppress long-T_2 water signal in white matter, leaving short-T_2 myelin protons to be imaged. Estimated myelin lipid fractions in white matter were 19.9% to 22.5% in the D_2O-exchanged spinal cord, and 18.1% to 23.5% in the non-exchanged spinal cord. Numerical simulations based on the myelin spectrum

[*]Corresponding Author: Tel: 215-662-7951. Fax: 215-662-7263. wehrli@mail.med.upenn.edu.
[4]Present Address: Translational and Molecular Imaging Institute, Icahn School of Medicine at Mount Sinai, 1470 Madison Ave., Suite S1-101, New York, NY 10029. Phone: (805) 304-8088, alan.seifert@mssm.edu
[†]These authors contributed equally to this work.

suggest that approximately 4.59% of the total myelin proton magnetization is observable by IR-ZTE at 3T due to T_2 decay and the inability to excite the shortest T_2^* components. Approximately 380 μm of point-spread function blurring is predicted, and ZTE images of the spinal cord acquired at 3T were consistent with this estimate.

Conclusion—In the present implementation, IR-UTE at 9.4T produced similar estimates of myelin concentration in D_2O-exchanged and non-exchanged spinal cord white matter. 3T data suggest that direct myelin imaging is feasible, but remaining challenging on clinical MR systems.

Keywords

MRI; myelin; UTE; ZTE; long-T2 suppression; white matter

1. Introduction

Myelin is an essential biomaterial responsible for electrically insulating axons and thus ensuring efficient neuronal signal transduction (van der Knaap and Valk, 2005). Image-based quantification of myelin has the potential to assess the severity of central nervous system (CNS) abnormalities such as demyelinating disorders and aid in the evaluation of the response to intervention (Paty et al., 2001; van der Knaap and Valk, 2005).

Most current MRI methods for detection of myelin abnormalities use magnetization transfer (MT) imaging or T_2 relaxometry. However, both methods constitute surrogate measures of myelin content, in that they exploit water's chemical or magnetic interaction with the myelin matrix, rather than directly imaging myelin matrix ^1H signal. One widely used technique is based on measurement of the magnetization transfer ratio (MTR). Schmierer et al. showed positive correlations of MTR with histologically determined axon densities in cadaveric brains from MS patients (Schmierer et al., 2004). Nevertheless, recent data by Vavasour et al (Vavasour et al., 2011) raise some concerns about the specificity of MTR. In an animal study of murine spinal cord, MTR was found to decrease after experimental demyelination via injection of lysolecithin, but failed to increase after histological evidence of remyelination (McCreary et al., 2009). More recently, bound proton fraction, derived from a quantitative two-pool MT model, has shown to be more predictive of myelin concentration than MTR (Samsonov et al.) but quantitative MT, like MTR, is still a proxy for myelin concentration.

Water in neural tissue exists in several pools, each with characteristic T_2 relaxation times corresponding to their respective microenvironments. T_2 relaxometry relies on quantification of the magnitude of a short T_2 water component ($T_2 \sim 20$ ms), the so-called "myelin water," which has been conjectured to arise from water trapped between the myelin bilayers (see, for instance, (Laule et al., 2007)). Since the other two long-T_2 water components, cerebrospinal fluid ($T_2 \sim 2$ s), and intracellular and extracellular water ($T_2 \sim 100$ ms) (Laule et al., 2007), relax much more slowly, they can be separated from myelin water by acquiring and analyzing the Carr-Purcell-Meiboom-Gill (CPMG) signal decay (MacKay et al., 1994). A T_2 spectrum is typically generated by non-negative least squares fitting of an array of exponential functions to the CPMG decay (Whittall and Mackay, 1989), and the myelin water fraction (MWF) then is estimated as the ratio of the area under the T_2 spectrum between the bounds of 20 ms and 50 ms, to the total area under the T_2 spectrum (Whittall et

al., 1997). However, there is some evidence that MWF does not always correlate with measured myelin content in normal tissue (Dula et al., 2010). Moreover, estimation of the T_2 spectrum from a superposition of amplitude-weighted exponentials (inverse Laplace transform) is a mathematically ill-posed problem (Epstein and Schotland, 2008) and typically requires high SNR, prior knowledge and appropriate regularization.

Direct detection of myelin would remove the complications of indirect methods (Wilhelm et al., 2012b). However, direct detection is challenging due to the extremely short lifetime of the myelin matrix proton MR signal (Horch et al., 2011) and interference from long-T_2 tissue-water signals. Some of the present authors previously showed the NMR spectral properties of myelin to be consistent with a lamellar liquid crystal, yielding a super-Lorentzian line shape with broad tails extending to about ±20 kHz, resulting in a lifetime of the transverse magnetization on the order of tens of microseconds (Wilhelm et al., 2012b). The work by Wilhelm et al. demonstrates that myelin extract and intact rat spinal cord myelin can be imaged by ultra-short echo time (UTE) MRI (Glover et al., 1992; Robson et al., 2003) on a laboratory 9.4T micro-imaging system. Early during the development of UTE, inversion-prepared UTE was explored at 1.5T to visualize the short-T_2 components purportedly arising from myelin in white matter in the brain of humans (Waldman et al., 2003). More recently, Du et al., using similar approaches, reported relative proton densities of the short-T_2 components of around 3–5% and a signal decay constant of 400 μs (Du et al., 2014).

In the present work, we further investigated the feasibility of direct myelin imaging, with a focus on quantification, by means of two solid-state imaging techniques. We first examined the potential of long-T_2 suppressed 3D UTE imaging at 9.4T to quantify myelin content in both deuterium oxide (D_2O)-exchanged and non-exchanged (i.e., in the natural ^{1}H-hydrated state) ovine spinal cord, using co-imaged reference samples containing various mass fractions of reconstituted myelin to generate a calibration curve. We then evaluated the performance of an alternative solid-state imaging method (Wu et al., 1999), more recently referred to as zero-echo time (ZTE) MRI (Weiger et al., 2013), given recent evidence that ZTE yields SNR superior to UTE in solid-state ^{31}P imaging with T_2 ~100 μs (Seifert et al., 2013). Lastly, we examine the feasibility of direct detection and quantification of myelin by ZTE-based methods at 3T under the gradient hardware constraints imposed by a typical clinical imaging system.

2. Methods

2.1. Sample Preparation

Myelin was extracted from ovine spinal cord by a sucrose gradient technique, in which the lipid bilayer structure has been shown to be fundamentally preserved (Norton, 1974). Following isolation, the crude myelin was dissolved in a (4:2:1) ternary mixture of chloroform, methanol, and water, to remove residual sucrose contaminants. Dissolution in the ternary mixture inverts the bilayer, thereby releasing embedded proteins, which comprise 30% of total ultrashort-T_2 signal in white matter, and yielding myelin lipids (Wessel and Flügge, 1984). The purified myelin lipids were removed from the chloroform phase using a rotary evaporator. The remaining myelin lipid residue was then re-suspended in distilled

water, frozen, and lyophilized to remove all remaining traces of solvent. Finally, the purified extract was suspended in 99.9% D_2O to achieve mass concentrations of 6%, 8%, 10%, 12% and 14%, which serve as reference samples for myelin quantification. The suspended extract self-assembles into liposomes consisting of concentric myelin lipid bilayers separated by thin layers of water (Hope et al., 1986).

Two 36-mm segments of ovine cervical spinal cord were dissected from the neck of a lamb slaughtered four days prior and stored at 4 °C. Before imaging, one segment was subjected to exchange with D_2O in three volumes of 12 mL D_2O-saline each over the course of 72 hours, while one was stored in 12 mL of H_2O-phosphate buffered saline. The process of D_2O exchange replaces all native (light) water in the tissue with D_2O, which is invisible on ${}^1H$ MRI, effectively removing the confounding effects of tissue water on myelin ${}^1H$ measurement.

2.2. Overview of MRI and Spectroscopic Experiments

Two sets of imaging experiments were performed. First, the quantification accuracy was examined on a laboratory micro-imaging system at 9.4T (Bruker Avance III 400) using a 1,000 mT/m 3-axis gradient set and a 25-mm diameter quadrature birdcage radiofrequency (RF) coil. In a second set of experiments, the performance of ZTE-based methods was evaluated at 3T on a clinical imaging system (TIM Trio; Siemens Medical Solutions, Erlangen, Germany) with 40 mT/m maximum gradient strength and a custom-built 4.5 cm-diameter, 8 cm-long, 3-turn transmit/receive solenoidal RF coil constructed of polytetrafluoroethylene (PTFE), which largely eliminates spurious ${}^1H$ signal.

Both myelin extracts and ovine spinal cord specimens were scanned with UTE and ZTE sequences. The pulse sequence diagrams are shown in Fig. 1. In order to minimize the interference from the non-myelin tissue components, an adiabatic inversion-recovery (IR)-based long-T_2 suppression, with a pass-band below approximately 1 ms, was employed. During the adiabatic preparation pulse, the long-T_2 magnetization of tissue water is inverted ($M_z < 0$), while the short-T_2 magnetization of myelin is saturated ($M_z \sim 0$) due to transverse relaxation during the pulse. After an inversion-recovery time (TI), the magnetization of tissue water is nulled ($M_z \sim 0$) by longitudinal relaxation, while the magnetization of myelin will have recovered to a positive ($M_z < 0$) and observable level. Prior work in the authors' laboratory showed that adiabatic IR provides highly uniform short-T_2 contrast, achieving highly effective long-T_2 suppression with near-immunity to B_1 inhomogeneity (Li et al., 2012).

At 9.4T, vendor-provided UTE and ZTE sequences were used, with a slight modification to UTE to enable IR preparation. At 3T, the samples were imaged with some of the present authors' previously developed long-T_2 suppressed IR-rZTE-PETRA (point-wise encoding time reduction with radial acquisition; an embodiment of the ZTE sequence designed for clinical scanners) (Li et al., 2016) and ZTE-PETRA (Grodzki et al., 2012) sequences.

In the resulting 9.4T images, due to the severely blurred signal arising from the plastic support of the RF coil, no region of background signal intensity is available in the images from which to calculate the noise signal. Signal-to-noise ratio (SNR) was therefore

calculated as the ratio of mean signal in a homogeneous myelin reference sample divided by the standard deviation within this sample. This definition of SNR therefore categorizes non-myelin background signal as noise.

Lastly, ^{1}H spectra were acquired on both instruments for the purpose of evaluating the line shape characteristics as described previously (Wilhelm et al., 2012b) and for estimating the detection sensitivity at 3T by solid-state MRI.

2.3. NMR Spectroscopy

A ^{1}H spectrum of the 14% myelin reference sample (approximately matching reported myelin concentration in white matter (van der Knaap and Valk, 2005)) was recorded at 9.4T using a 5 mm spectroscopy RF probe to ensure that the lipid bilayer structure was preserved (bandwidth = 100 kHz, number of averages = 256, number of data points = 262,144, TR = 3.6 s, FA = 90°, pulse duration = 9.6 μs). A spectrum of intact D_2O-exchanged ovine spinal cord was also acquired at 3T (bandwidth = 250 kHz, number of averages = 64, number of data points = 4096, 6 points dropped due to transmit/receive switching, TR = 6.144 s, FA = 27°, pulse duration = 20 μs, group delay = 48 μs). Both spectra were subsequently analyzed to determine the various transverse relaxation components making up the super-Lorentzian line shape.

2.4. Myelin Imaging with ZTE Sequences

Inclusion of ZTE imaging was motivated by the superior SNR of ZTE at extremely short T_2, as shown in some of the authors' previous work (Seifert et al., 2013). In ZTE, there is a shorter delay between excitation of signal and acquisition of any given k-space point, compared to UTE (Weiger and Pruessmann, 2012). At 9.4T, a commercial ZTE sequence was used to simultaneously image both non-exchanged and D_2O-exchanged ovine spinal cords, and the five D_2O-suspended myelin reference samples described above, with the following parameters: TR = 2 ms, 2 μs pulse duration, FA = 2.5° (at maximum pulse amplitude), 3.2 μs dwell time, 204.8 μs encoding duration, 230.1 mT/m maximum gradient amplitude, 51,897 half-projections (no undersampling), $32 \times 32 \times 96$ mm^3 FOV, $250 \times 250 \times 750$ μm^3 nominal voxel size, scan time = 27.4 min.

A D_2O-exchanged spinal cord specimen and the set of myelin extract samples were also scanned separately in a 15-mm RF probe to provide high-resolution RARE and ZTE images for visualization purposes only. In these ZTE images, the flip angle was increased to 4.1° (maximum achievable with this smaller RF probe) and the encoding matrices were altered to increase voxel resolution, but all other sequence parameters were identical to images acquired using the 25-mm RF probe.

For comparison, a commercial UTE sequence was also employed at 9.4T with the following parameters: TR = 2 ms, TE = 12.5 μs, 5.12 μs pulse duration, FA = 4.7°, 3.2 μs dwell time, 204.8 μs encoding duration, 230.1 mT/m maximum gradient amplitude, 51,360 half-projections (no undersampling), $32 \times 32 \times 96$ mm^3 FOV, $250 \times 250 \times 750$ μm^3 nominal voxel size, scan time = 27.7 min.

2.5. Myelin Quantification with Long-T_2 Suppressed UTE Imaging

Prior work in the authors' laboratory showed the UTE signal amplitude to be strongly correlated with the mass fraction of myelin suspended in D_2O (R^2=0.98). In the present work we investigated the potential of UTE imaging with adiabatic IR-based long-T_2 suppression for quantification of myelin in non-exchanged white matter with an experimental set-up similar to that used in (Wilhelm et al., 2012b).

The non-exchanged ovine spinal cord was scanned at 9.4T with IR-UTE along with the myelin reference samples using the following scan parameters: TR = 200 ms, TI = 90 ms; and a hyperbolic secant (HS_1) adiabatic inversion pulse with 5-kHz bandwidth and 5-ms pulse duration. The optimal TI was predicted by Bloch equation simulations, and verified empirically by performing additional scans at various TIs surrounding the optimal value to verify the nulling of long-T_2 signal. Following each inversion, a single UTE readout was performed at TE = 12.5 μs, 3.2μs dwell time, 204.8 μs encoding duration, and 230.1 mT/m maximum gradient amplitude. The UTE excitation pulse duration was extended to 40 μs (lifetime of a significant fraction of the myelin proton signal), and the pulse amplitude was increased to maximum, yielding a flip angle of 50°. A total of 51,360 half-projections (no undersampling) were acquired in 3.1 hours. Images with a $32 \times 32 \times 96$ mm^3 FOV were reconstructed at a voxel size of $250 \times 250 \times 750$μm^3.

After image reconstruction, the myelin fractions in the spinal cord white matter were determined from the calibration equation derived from the association between MR signals of the reference samples and their known myelin fractions. Because the reference samples do not contain myelin proteins (which comprise about 30% of macromolecular volume in white matter), while the intact spinal cord white matter does contain these additional proteins, a correction factor of 0.7 was applied to the measured intensity in the spinal cord to determine myelin lipid fraction specifically.

Insertion of an adiabatic IR preparation into this commercial ZTE sequence pulse proved not to be effective. As previously pointed out, the presence of the imaging gradient in ZTE mandates an excitation RF pulse short enough (i.e., an excitation bandwidth broad enough) to uniformly excite the spins across the FOV, so as to avoid spatial selectivity and the resulting blurring and shading artifacts (Li et al., 2014). However, in order to maximize myelin proton SNR, the optimal flip angle is 90° (since the myelin protons are also saturated by the adiabatic pulse in each TR). At a given readout bandwidth, such a flip angle requirement could not be reconciled with the limitation on pulse duration due to limited peak RF power. Therefore, the desired flip angle could only be achieved in ZTE by prolonging both the pulse duration and the readout dwell time (i.e., decreasing the readout bandwidth), which, in turn, requires the readout gradient amplitude to be decreased by the same factor to maintain the FOV. However, this decreased readout gradient amplitude was found to introduce unacceptable blurring artifacts due to T_2 relaxation during readout and the resulting point spread function (PSF) broadening.

Some of these limitations in ZTE can be alleviated with a custom-designed multiple-readout pulse sequence as described in Section 2.2 above and references (Li et al., 2016) and

(Weiger et al., 2015). No such pulse sequence was available for the experiments conducted on the 9.4T micro-imaging system.

2.6. Feasibility of Myelin Imaging on Clinical MRI Systems

To assess feasibility of myelin imaging under the hardware constraints imposed by clinical imaging instrumentation, numerical simulations were first performed to project the fraction of observable myelin magnetization. The starting point was to acquire and examine the myelin spectrum in terms of its multiple T_2^* components, then perform simulations to predict the fraction of total magnetization that is observable in a ZTE pulse sequence, and finally perform imaging experiments at 3T with a custom-designed RF coil on ovine spinal cord specimens analogous to the work on the 9.4T laboratory imaging system.

The T_2^* spectrum of myelin was estimated by fitting the ^{1}H spectrum acquired at 9.4T to a sum of four super-Lorentzian (SL) functions, one for each of the distinct chemical shift environments (Wilhelm et al., 2012a). The SL function, $L(\omega)$, is based on the work by Wennerstrom on the proton NMR line shape of lamellar liquid crystals (Wennerstrom, 1973), and was constructed as:

$$L(\omega) = \int_0^{\pi/2} \frac{\sin(\theta)}{|3\cos^2(\theta) - 1|} f\left(\frac{\omega - \omega_0}{|3\cos^2(\theta) - 1|}\right) d\theta \qquad [1]$$

Here, ω is the chemical shift centered at ω_0, θ is the angle of the lipid bilayer surface normal with respect to B_0, and $f(\omega-\omega_0)$ is set to be a Lorentzian. Four SLs with different chemical shifts were used to represent alkyl chain methylenes from fatty acids, cholesterol alkyl chain methylenes, terminal methyls, and choline, while a single Lorentzian was used to model residual monodeuterium oxide (HDO). The T_2^* spectrum was computed from the widths and intensities of the individual Lorentzians line-shapes comprising the super-Lorentzian. The T_2^* spectrum was further corrected for transverse relaxation of each T_2^* component during the 16-μs RF excitation pulse. We expected the T_2^* spectrum at 3T to differ only minimally from that at 9.4T because the primary contribution to the line width is dipole-dipole coupling.

Based on the T_2^* spectrum, the observable fraction of the total myelin proton magnetization was estimated for an IR-ZTE-PETRA sequence via Bloch equation simulations for various ranges of acquisition parameters. Including the effect of the adiabatic inversion pulse and assuming the magnetization to have reached a steady state, the observable myelin signal was calculated as the sum of all T_2^* component signals:

$$S = \sum_i M_{0,i} f_{xy,i} \frac{1 - (1 - f_{z,\mathrm{HS},i})\exp\left(\frac{-\mathrm{TI}}{T_1}\right) - f_{z,\mathrm{HS},i}\exp\left(\frac{-(\mathrm{TR}-t_{\mathrm{HS}})}{T_1}\right)}{1 - f_{z,\mathrm{HS},i} f_{z,i}\exp\left(\frac{-(\mathrm{TR}-t_{\mathrm{HS}})}{T_1}\right)} \exp\left(\frac{-\mathrm{TE}}{T_{2,i}^*}\right) \qquad [2]$$

Here, the index i denotes a single T_2^* component, $M_{0,i}$ is the value of the T_2^* spectrum at $T_2^*{}_i$, $f_{xy,i}$ and $f_{z,i}$ represent the transverse and longitudinal magnetization responses to the

rectangular excitation pulse, calculated analytically for each T_2^* component (Sussman et al., 1998), and $f_{z,HS,i}$ is the longitudinal magnetization response to the adiabatic inversion pulse, computed numerically for each T_2^* component. TI is the inversion time, defined as the time interval between the end of the adiabatic pulse and the start of the rectangular excitation pulse, t_{HS} is the adiabatic inversion pulse duration, TR is the repetition time, and TE is the echo time (defined as the time interval between the end of hard pulse and the start of signal acquisition, i.e. the first readout point).

Parameters chosen are those of a typical IR-ZTE-PETRA scan protocol: hard pulse duration = 32 μs; flip angle = 40°; TE (more specifically, transmit/receive dead time) = 48 μs; TR = 300 ms; TI = 120 ms, hyperbolic secant (HS) inversion pulse duration = 5 ms; HS bandwidth = 5,000 Hz; number of HS pulse samples = 500; T_1 = 660 ms (prior work on D_2O suspended myelin lipid had yielded a composite T_1 value of 0.66s at 9.4T (Wilhelm et al., 2012b)). Observability was defined as S/M_0, where M_0 represents the total equilibrium magnetization, i.e., the integral of the T_2^* spectrum.

Estimates of the observable fraction, S/M_0, were further computed for RF pulse durations ranging from 8 μs to 200 μs, flip angles from 3° to 90°, and TEs from 2 μs to 64 μs. These computations were performed in Matlab R2015b (Mathworks, Natick, MA, USA) on a high-performance image analysis server (32 CPU cores, 256 GB RAM, Linux Ubuntu 13.10, requiring 50 hours total processing time).

The full-width at half maximum (FWHM) of the PSF, a measure of the extent of expected blurring due to signal attenuation during readout, was computed for a 3D ZTE pulse sequence. Using the T_2^* distribution of observable myelin signal calculated using Equation 2, and assuming gradient strengths of G = 36.7 mT/m at 3 T and G = 230.9 mT/m at 9.4 T, the modulation-transfer functions (MTFs) at each field strength were evaluated and the PSFs were obtained via a 1D Fourier-transform of the MTF. The relationship between time and k-space is given as k = $(\gamma/2\pi)\cdot$G$\cdot$t.

Lastly, the feasibility of direct detection of myelin was examined experimentally at 3T. A D_2O-exchanged ovine spinal cord was imaged with a ZTE-PETRA sequence, with the following parameters: TR = 7 ms, 16 μs pulse duration, FA = 8.3°, 8 μs dwell time, 48 μs transmit/receive dead time, 640 μs encoding duration, 36.7 mT/m gradient amplitude, 25,000 half-projections (no undersampling), $80 \times 80 \times 80$ mm^3 FOV, $1 \times 1 \times 1$ mm^3 voxel size, 4 averages, 12.7 min total scan time. The ovine spinal cord was subsequently scanned with an IR-rapid ZTE (rZTE)-PETRA sequence ('rapid' denoting multiple readouts per inversion) derived from the above parent ZTE-PETRA sequence by the addition of a hyperbolic secant (HS) adiabatic inversion pulse of 5-kHz bandwidth and 5-ms pulse duration. To improve scan efficiency, seven radial spokes, with a repetition interval of 2 ms and an optimized set of excitation flip angles ranging from 22.5° to 40° (Li et al., 2016) were acquired after each adiabatic inversion (hence the designation 'rapid') with TR = 300 ms and TI = 120 ms. Other scan parameters were modified as follows: 32 μs pulse duration (to allow for an increased flip angle), 16 μs dwell time (to compensate for an increased pulse duration), 48 μs transmit/receive dead time, 640 μs encoding duration, 18.3 mT/m gradient amplitude (to compensate for the increased pulse duration and dwell time), 25,000 half-projections (no

undersampling), $80 \times 80 \times 80$ mm^3 FOV, $1 \times 1 \times 1$ mm^3 voxel size, 1 average, 18.4 min total scan time.

This multiple-acquisition-per-inversion enhancement renders IR-rZTE-PETRA feasible at 3T, while such an enhancement was not available at 9.4T, thereby precluding a comparison between the two field strengths. The low gradient slew rates available on a 3T human scanner, combined with the extremely short T_2* of myelin, result in severe PSF blurring, leading to featureless and uninterpretable UTE images in these small spinal cord specimens. For this reason, only ZTE-PETRA and IR-rZTE-PETRA were performed at 3T.

3. Results

The ^{1}H spectrum of the myelin reference sample (purified extract-D_2O suspension) at 9.4T in Fig. 2a shows a broad resonance with relatively narrow components centered at the lipid frequency, consistent with a dipolar broadened liquid-crystalline lipid system as reported previously (Wilhelm et al., 2012b). The spectral line shape of the ovine spinal cord in Fig. 2c after D_2O exchange has qualitatively similar characteristics, specifically, the same super-Lorentzian features and a sharper peak arising from residual HDO. The similarity of the two spectra is supported by the T_2* spectra in Figs. 2b and d.

The bulk of spectral power resides between about 5 and 30μs (Fig. 2b), and is slightly longer for the spinal cord, as the tissue also contains gray matter and other fast-relaxing constituents (Fig. 2d). It is therefore not appropriate to characterize transverse relaxation of myelin in terms of a single time constant (even though measurements obtained using longer excitation pulses may suggest a mono-exponential decay (Sheth et al., 2016)). A mono-exponential appearance is merely the result of the inability of RF pulses longer than the signal lifetime to excite the shortest T_2* components.

A mono-exponential fit to the first 2 ms of 9.4T FID data used to generate Fig. 2a yields a T_2* of 117 μs and $R^2 = 0.915$. A mono-exponential fit to the first 2 ms of 3T data used to generate Fig. 2c yields a T_2* of 238 ms and $R^2 = 0.994$. The longer fitted T_2* value and higher R^2 at 3T are due to greater losses of short-T_2* signal during the longer RF pulse and transmit/receive dead time. Fitting to only the first 2 ms of data reduces the influence of any residual HDO, which has much longer T_2*. In contrast, the R^2 values of the super-Lorentzian fits in Fig. 2 are 0.9992 and 0.9990 at 3T and 9.4T, respectively. These results are consistent with the known physical properties of the liquid-crystalline myelin lipid (Wilhelm et al., 2012b).

As assessed using Equation 2, taking into account the multiple T_2* components and under the typical parameters stated in the Methods section (flip angle = 40°, pulse duration = 32 μs, and dead time = 48 μs), an IR-ZTE-PETRA pulse sequence would be able to observe 4.59% of the equilibrium magnetization. Under an extremely optimistic set of parameters (flip angle = 90°, pulse duration = 16 μs, and dead time = 8 μs), the same pulse sequence would be able to observe 11.7% of the equilibrium magnetization. Fig. 3 shows plots of estimates of the observable fraction of M_0 for ranges of flip angles, RF pulse durations, and dead times.

Fig. 4 shows the MTFs (Figs. 4a and c) and PSFs (Figs. 4b and d) of myelin ^{1}H signal at 9.4 T and 3 T. The FWHM of the PSF of observable signal was 380 μm at 3 T, using a 36.7 mT/m encoding gradient, and 64 μm at 9.4 T, using a 230.9 mT/m encoding gradient.

Fig. 5 shows a series of representative images of ovine spinal cord and myelin extract reference samples, including a high-resolution 9.4T RARE image of the spinal cord specimen, for anatomic reference (Fig. 5a). Fig. 5b displays a ZTE image of the same specimen, using a 15-mm RF coil in this case, after D_2O exchange of tissue water at the same anatomic location. Contrast is determined by myelin densities as borne out by the lower intensity in the gray matter. ZTE also captures signal from the plastic structure of the RF coil in the periphery of the image. A ZTE image of various concentrations of myelin extract in D_2O shows the method's ability to differentiate the range of myelin concentrations expected in neural white matter, along with two samples of 10% H_2O and 90% D_2O, one being doped with 14 mM $MnCl_2$ (Fig. 5c). Intensities scale as expected with the actual myelin concentrations (Fig. 5d). Figs. 5e and f show ZTE-PETRA and IR-rZTE-PETRA images of the D_2O-exchanged spinal cord specimen, acquired on a 3T clinical scanner with a custom-built ^{1}H-free solenoidal coil. Even though the voxel size is much larger and PSF blurring is severe due to low gradient amplitudes, some anatomic features are apparent.

Fig. 6 compares UTE, ZTE and IR-UTE images at 9.4T of the same spinal cord specimen in the non-exchanged and D_2O-exchanged state. Structural features are only faintly detectable (that is, there is low contrast between gray and white matter) in the non-exchanged state without tissue water suppression since the images are largely proton density weighted (Figs 6a and b). While tissue water density is well known to be greater in gray matter than in white matter (Wehrli et al., 1984), the opposite is the case for myelin density, presumably leading to a contrast cancellation effect. The best myelin contrast is achieved in the IR-UTE image of the non-exchanged cord, clearly showing greater density, for instance, in the dorsal columns, and high contrast between gray matter and white matter in general (Fig. 6c). Contrast is less pronounced in the images obtained after D_2O exchange of tissue water (Figs. 6d – f) although a slight improvement is visible in IR-UTE (Fig. 6f), suggesting the presence of residual monodeuterium oxide (HDO). This phenomenon will be addressed in more detail in the discussion section. SNRs calculated in the 14% myelin extract sample in the non-exchanged ZTE, UTE, and IR-UTE images were 23, 7.8, and 18, respectively, and SNRs in the D_2O-exchanged ZTE, UTE, and IR-UTE images were 24, 20, and 19, respectively. Severe Gibbs ringing is visible emanating from the long-T_2 water in the non-exchanged UTE image (Fig. 6b), leading to low SNR in that image; SNRs calculated in the D_2O-exchanged images are, therefore, most reliable. SNR in the D_2O-exchanged ZTE image is 19% higher than in the D_2O-exchanged UTE image.

Fig. 7 illustrates the process of image-based quantification of white matter myelin density based on IR-UTE images of non-exchanged and D_2O-exchanged spinal cords and myelin extract reference samples at 9.4T. Myelin extract in the 10% reference sample was found to have significantly precipitated out of suspension, and could not be re-suspended by agitation. This sample's signal intensity was inhomogeneous and did not correspond to its concentration; the 10% point was therefore excluded from the calibration. All other samples were stably suspended and produced homogeneous signal intensity. The significant y-

intercept in the calculated linear regressions is attributed to long-range blurring of the shortest T_2^* components of myelin, the plastic housing of the RF coil, and any other ^{1}H-containing materials placed near conductors within the magnetic field.

Myelin density in three white matter regions of interest (ROIs) was found to be 18.1% to 23.5% in the non-exchanged cord, and 19.9% to 22.5% in the D_2O-exchanged cord, after correction for the residual proteins present in the intact spinal cord neural tissue (comprising approximately 30% of the short-T_2 signal in the cord) (Morell and Quarles, 1999). The highest myelin density was found in the dorsal columns, as expected. These ROIs are drawn close to the gray matter to avoid bias in quantification due to a low-spatial-frequency reconstruction artifact in Fig. 7d, visible as a ring of low signal intensity at the outer boundary of the spinal cord. The agreement of these measurements between non-exchanged and D_2O-exchanged cords substantiates the quality of tissue water suppression in the white matter, though this is not the case in the gray matter.

4. Discussion

The potential of 3D UTE and ZTE MRI for direct myelin quantification was evaluated on ovine myelin extracts and spinal cords ex vivo. In the present implementation, it was found that IR preparation effectively suppresses the long-T_2 signal, with IR-UTE currently achieving the most promising results at 9.4T. Myelin images were also acquired on a 3T clinical scanner using custom-designed ZTE-PETRA and IR-rZTE-PETRA pulse sequences.

A major limitation is achievable image SNR, considering that tissue water ^{1}H concentration is on the order of 100 M, while the concentration of detectable myelin ^{1}H is only about 700 mM. Although this concentration is an order of magnitude larger than typical metabolite concentrations routinely examined by NMR spectroscopy, myelin is not spectrally homogeneous. Another concern is the limited specificity of the method, since myelin detection is solely based on its T_2^* properties. There are other possible non-myelin short-T_2^* sources that could contribute to the ZTE signal, including glial cell membranes, which would be indistinguishable from myelin based on T_2^* alone (Waldman et al., 2003). Residual long-T_2 signal, due to imperfect suppression, may be misclassified as short-T_2^* signal and, hence, may also be falsely identified as myelin.

Myelin proteins (the principal one being myelin basic protein; molecular weight ~ 18 kDa), comprise approximately 30% of intact white matter by volume (Morell and Quarles, 1999). However, it does not necessarily follow that these proteins contribute 30% of ZTE signal in intact white matter; T_2 of some of the protein signals may be longer than those in myelin, in which case proteins may contribute more than 30% of ZTE signal, necessitating a smaller correction factor than the value of 0.7 used in this work to achieve absolute quantification. Determination of the precise correction factor would require detailed study of the relaxation properties of the principal myelin protein constituents, which is beyond the intended scope of the present work. Nevertheless, error in the correction factor would produce a constant bias in the quantification, and therefore would not affect the strength of the correspondence of signal intensity to myelin density. Conclusions drawn based on comparisons between

images of D_2O-exchanged and non-exchanged specimens, as in Fig. 7, would not be affected by such biases.

Although SNR obtained at 9.4T with plain ZTE (i.e. without long-T_2 suppression) was superior to plain UTE data, IR-ZTE with long-T_2 suppression suffers from a limit on the achievable excitation flip angle secondary to the limit placed on excitation RF pulse duration by the presence of the readout gradient, necessitating additional pulse sequence-based enhancements, such as multiple readouts per inversion. IR-ZTE, therefore, cannot be directly compared to an optimized IR-UTE protocol, where the duration of the excitation pulse is more flexible, and the flip angle can be increased to the optimal 90°. This problem could be mitigated on our 3T clinical scanner by applying multiple readouts per inversion in an IR-rZTE-PETRA sequence (Li et al., 2016), and has also been reported on a small-bore imager (Weiger et al., 2015), but this sequence enhancement could not be implemented on the 9.4T system used in this study.

The long-T_2 suppression module limits the observability of the myelin ^1H signal. Specifically, the 5-ms adiabatic inversion pulse is far longer than the lifetime of the myelin ^1H signal, and so the pulse saturates (i.e., zeroes) the magnetization of myelin protons. This means that the available myelin signal results entirely from the magnetization recovered via longitudinal relaxation during the inversion time. Given the relatively long T_1 of myelin proton signal (660 ms, calculated from myelin lipid extract suspended in D_2O), the fraction of recovered longitudinal magnetization is only about 15% of the equilibrium magnetization, even before losses incurred due to transverse relaxation during the RF pulse and TE are considered.

Saturation of the myelin ^1H signal by the adiabatic inversion pulse applied in each TR also means that there is no reduction in steady-state longitudinal magnetization as the excitation flip angle is increased; any magnetization that is not excited and encoded in a given TR period is wasted, as it will be annihilated by the following long-T_2 suppression pulse. It is therefore advantageous to apply multiple readouts per TR, as described above, as long as the series of N excitation flip angles is optimized to produce equal transverse magnetization from a progressively depleted pool of longitudinal magnetization. The only caveat is that only the Nth excitation pulse in this series can utilize the full RF excitation capabilities of the scanner hardware, and pulses 1 through N-1 must be set to lower flip angles for this condition of constant transverse magnetization per excitation to be met (Li et al., 2016). The fraction of M_0 observed by each of these multiple excitations per TR is equal to that predicted by Equation 2 using the flip angle of the first pulse in the series, under two assumptions: (1) that the series of flip angles is optimized to produce equal transverse magnetization per excitation, (2) the longitudinal magnetization of myelin ^1H is saturated by the HS pulse and, therefore, reset in each TR (confirmed by numerical calculation of $f_{z,HS}$, which is ~0 for $T_2^* < 1$ ms).

It is best practice in ZTE to set the excitation RF pulse to maximum power so that pulse duration can be minimized for a given flip angle. This condition maps to a diagonal in the plot of observable signal fraction versus flip angle and pulse duration (Fig. 3a), the slope of which is proportional to the maximum power achievable by the scanner's RF hardware. The

upper left quadrant of Fig. 3a, which contains the highest observable signal fractions, would require unrealistically high RF power. The choice of flip angle is, therefore, dictated by the maximum tolerable pulse duration (which, in turn, depends on multiple other parameters, including FOV and readout gradient strength). In interpreting Fig. 3b, in which the observable fraction is plotted against flip angle and TE, we note that in ZTE there is no TE, per se; instead, data acquisition begins after the transmit/receive dead time has elapsed following the RF excitation pulse. Using this logic, we arrive at a single optimal set of values for pulse duration, flip angle, and TE.

The efficacy of long-T_2 suppression is sensitive to the composite T_1 of the tissue water to be suppressed. This dependence is visible in the rather different gray matter signal intensities between non-exchanged and D_2O-exchanged cords in Figs. 7d, h, and in the residual bulk water outside the cord in Fig. 7d. Tissue water in gray matter has a longer T_1 than tissue water in white matter. Tissue water longitudinal magnetization in white matter, with its relatively short T_1, is optimally nulled by the chosen TI, leaving myelin ^{1}H with positive longitudinal magnetization. Free water outside the spinal cord, whose T_1 is longer than white matter tissue water, is not exactly nulled, and therefore should have residual negative longitudinal magnetization at time TI, which manifests as positive signal on a magnitude image. Gray matter tissue water, whose T_1 is also longer than that of white matter, is also not exactly nulled, and therefore should also have residual negative longitudinal magnetization at time TI. Gray matter, however, also contains myelin (although less than white matter), whose protons have positive longitudinal magnetization at time TI. The presence of both gray matter tissue water with negative longitudinal magnetization at time TI, and myelin ^{1}H with positive longitudinal magnetization at time TI, causes signal from these two components to cancel within voxels in the gray matter, leading to lower signal on a magnitude image of non-exchanged spinal cord than on a magnitude image of D_2O-exchanged spinal cord.

For quantification of myelin in healthy white matter, TI can be tuned to most effectively suppress white matter tissue water. However, since T_1 is largely determined by cross-relaxation involving myelin (Henkelman et al., 2001), any reduction in myelin density (e.g. in the setting of inflammation or demyelination, or in gray matter), would require TI to be re-tuned to optimally null tissue water due to the differences in bulk water T_1 in these tissues, and precise quantification may not be achievable simultaneously in multiple tissues.

Long-T_2 ^{1}H signal in UTE and ZTE sequences can also be attenuated by subtracting a second-echo image, which would be primarily composed of signal from long-T_2* sources, from the image containing both short-T_2* myelin signal and long-T_2* water signal. Similarly, a UTE image acquired with a long, low-amplitude RF pulse, which would successfully excite only long-T_2 signal, could be subtracted from a UTE image acquired with a short, high-amplitude RF pulse, which would excite both long- and short-T_2 signal (Johnson et al., 2017). The choice of adiabatic inversion-recovery for this work is based on the sharper transition between T_2 passband and stop-band, and the selectivity for T_2, rather than T_2* (myelin and non-myelin ^{1}H signals are separated by a greater factor in the T_2 than in the T_2* dimension) (Horch et al., 2012).

As stated earlier, a recent report suggests the feasibility of direct detection of the short-T_2 components in white matter in the human brain at 3 T by means of a 2D IR-UTE sequence (Du et al., 2014). Although the enhanced short-T_2 contrast between white matter and gray matter and the measured T_2* values in the white matter region after application of long-T_2 suppression imply that 2D IR-UTE is also able to capture short-T_2 components in the brain, it is uncertain whether the detected signal is predominantly from myelin. Since transverse relaxation during excitation may be severe due to the relatively long slice-selective RF pulse, 2D IR-UTE detects only the portion of myelin protons with longer signal life-times. Such T_2-selective excitation may also account for a longer apparent myelin T_2* of ~300 μs measured by Sheth et al (Sheth et al., 2016). Again, because of the highly non-Lorentzian line shape of the myelin resonance, the concept of a single T_2* value is not applicable.

The maximum gradient strength on the 3T scanner used is 36.7 mT/m, which is an order of magnitude below that of the 9.4T spectrometer used in this work[†], resulting in considerably greater signal decay during spatial encoding, which in turn exacerbates PSF blurring in both UTE and ZTE. Emerging dedicated RF and gradient coils will significantly enhance the potential for myelin imaging in the human central nervous system. The gradient slew rates of clinical scanners are also much lower than those of the 9.4T micro-imaging system, leading to significant additional T_2* decay during the long gradient ramps in UTE, further broadening the PSF, thereby leading to substantially inferior UTE and IR-UTE image quality. These two technical constraints, software-imposed at 9.4T and hardware imposed at 3T, limit IR-rZTE to 3T only, and UTE and IR-UTE to 9.4T only, in this study.

It is important to note that the FWHM of the PSF is not an appropriate criterion for assessing intrinsic spatial resolution of myelin imaging methods, due to the distinguishing properties of Lorentzian and super-Lorentzian lineshapes. The latter has a sharper central peak and broader, elevated tails relative to the Lorentzian. This means that the proportion of signal captured within the FWHM of the peak is much less than for a Lorentzian, and image blurring will appear more significant than suggested by the FWHM of the PSF. Indeed, our predicted value of 380 μm at 3T suggests finer resolution than is actually achievable. Nevertheless, a voxel size of $250 \times 250 \times 750$ μm^3 will allow the longer-T_2* components to be finely resolved, although shorter-T_2* signal will still blur across several voxels.

In the present work, a custom solenoidal RF coil was used at 3T. This coil provides much greater RF transmit amplitude and receive sensitivity than achievable with standard clinical RF coils. The SNR efficiency achievable using a standard human RF coil at 3T, therefore, will be substantially lower than what could be achieved in the present study. Greater averaging and/or further sequence-based improvements will be necessary to increase the SNR using standard coils. The above limitations, while not insurmountable in principle, nevertheless suggest direct imaging and quantification of myelin in humans in vivo to remain challenging for the time being.

[†]Even though the nominal gradient strength of the system is 1,000 mT/m on all three axes, the highest gradient achieved was 230.9 mT/m due to duty cycle limits.

Lastly, development of enhanced hardware capabilities currently in progress on clinical systems may enable implementation of line-narrowing techniques (see, for example, (Frey et al., 2012)). Such approaches, at the present only possible on laboratory spectrometer/ imaging systems, have the potential to increase the effective T_2^* of myelin protons by several orders of magnitude, but the specific absorption rate (SAR) of RF energy may be a limiting factor. Besides line-narrowing techniques, it is possible to excite a small portion of a broad resonance by narrow-banded selective RF pulses, as shown, for instance, by Khitrin et al. (Khitrin, 2011), and more recently, in an imaging implementation for the detection of short-T_2 protons in bone (Zhang et al., 2013). However, the separation of these signals from long-T_2 tissue water components would remain challenging.

5. Conclusions

In the present implementation, appropriately designed IR-preparation suppression pulses effectively suppress the long-T_2 signal in white matter. Myelin density maps produced at 9.4T in both non-exchanged and D_2O-exchanged cords show the expected contrast between gray and white matter, and the densities measured in three regions of white matter are in the range of 18.1% to 23.5% and are consistent between the non-exchanged and D_2O-exchanged cords. Feasibility of direct myelin imaging was also shown on a 3T clinical scanner using custom-designed ZTE-PETRA and IR-rZTE-PETRA pulse sequences.

Acknowledgments

References

Du J, Ma GL, Li SH, Carl M, Szeverenyi NM, VandenBerg S, Corey-Bloom J, Bydder GM. Ultrashort echo time (UTE) magnetic resonance imaging of the short T2 components in white matter of the brain using a clinical 3T scanner. Neuroimage. 2014; 87:32–41. [PubMed: 24188809]

Dula AN, Gochberg DF, Valentine HL, Valentine WM, Does MD. Multiexponential T2, magnetization transfer, and quantitative histology in white matter tracts of rat spinal cord. Mag. Res. Med. 2010; 63:902–909.

Epstein CL, Schotland J. The bad truth about Laplace's transform. SIAM Rev. 2008; 50:504.

Frey MA, Michaud M, VanHouten JN, Insogna KL, Madri JA, Barrett SE. Phosphorus-31 MRI of hard and soft solids using quadratic echo line-narrowing. Proceedings of the National Academy of Sciences of the United States of America. 2012; 109:5190–5195. [PubMed: 22431609]

Glover GH, Pauly JM, Bradshaw KM. Boron-11 imaging with a three-dimensional reconstruction method. Journal of Magnetic Resonance Imaging. 1992; 2:47–52. [PubMed: 1623280]

Grodzki DM, Jakob PM, Heismann B. Ultrashort echo time imaging using pointwise encoding time reduction with radial acquisition (PETRA). Magn Reson Med. 2012; 67:510–518. [PubMed: 21721039]

Henkelman RM, Stanisz GJ, Graham SJ. Magnetization transfer in MRI: a review. NMR Biomed. 2001; 14:57–64. [PubMed: 11320533]

Hope MJ, Bally MB, Mayer LD, Janoff AS, Cullis PR. Generation of multilamellar and unilamellar phospholipid vesicles. Chemistry and Physics of Lipids. 1986; 40:89–107.

Horch RA, Gochberg DF, Nyman JS, Does MD. Clinically compatible MRI strategies for discriminating bound and pore water in cortical bone. Magn Reson Med. 2012; 68:1774–1784. [PubMed: 22294340]

Horch RA, Gore JC, Does MD. Origins of the ultrashort-T2 1H NMR signals in myelinated nerve: A direct measure of myelin content? Mag. Res. Med. 2011; 66:24–31.

Johnson EM, Vyas U, Ghanouni P, Pauly KB, Pauly JM. Improved cortical bone specificity in UTE MR Imaging. Magn Reson Med. 2017; 77:684–695. [PubMed: 26972442]

Khitrin AK. Selective excitation of homogeneous spectral lines. J Chem Phys. 2011; 134:154502. [PubMed: 21513390]

Laule C, Vavasour IM, Kolind SH, Li DKB, Traboulsee TL, Moore GRW, MacKay AL. Magnetic resonance imaging of myelin. Neurotherapeutics. 2007; 4:460–484. [PubMed: 17599712]

Li C, Magland JF, Rad HS, Song HK, Wehrli FW. Comparison of optimized soft-tissue suppression schemes for ultrashort echo time MRI. Magn Reson Med. 2012; 68:680–689. [PubMed: 22161636]

Li C, Magland JF, Seifert AC, Wehrli FW. Correction of excitation profile in Zero Echo Time (ZTE) imaging using quadratic phase-modulated RF pulse excitation and iterative reconstruction. IEEE Trans Med Imaging. 2014; 33:961–969. [PubMed: 24710164]

Li C, Magland JF, Zhao X, Seifert AC, Wehrli FW. Selective in vivo bone imaging with long-T suppressed PETRA MRI. Magn Reson Med. 2016

MacKay A, Whittall K, Adler J, Li D, Paty D, Graeb D. In vivo visualization of myelin water in brain by magnetic resonance. Magn Reson Med. 1994; 31:673–677. [PubMed: 8057820]

McCreary CR, Bjarnason Ta, Skihar V, Mitchell JR, Yong VW, Dunn JF. Multiexponential T2 and magnetization transfer MRI of demyelination and remyelination in murine spinal cord. NeuroImage. 2009; 45:1173–1182. [PubMed: 19349232]

Morell, P., Quarles, R. Characteristic Composition of Myelin. In: Siegel, G.Agranoff, B., Albers, R., editors. Basic Neurochemistry: Molecular, Cellular and Medical Aspects. 6. Lippincott-Raven; Philadelphia: 1999.

Norton WT. Isolation of myelin from nerve tissue. Methods Enzymol. 1974; 31:435–444. [PubMed: 4370711]

Paty DW, Li DK, Group, U.M.M.S., Group, I.M.S.S. Interferon beta-lb is effective in relapsing-remitting multiple sclerosis. II. MRI analysis results of a multicenter, randomized, double-blind, placebo-controlled trial. 1993 [classical article]. Neurology. 2001; 57:S10–15. [PubMed: 11902589]

Robson MD, Gatehouse PD, Bydder M, Bydder GM. Magnetic resonance: An introduction to ultrashort TE (UTE) imaging. J. Comput. Assist. Tomogr. 2003; 27:825–846. [PubMed: 14600447]

Samsonov A, Alexander AL, Mossahebi P, Wu YC, Duncan ID, Field AS. Quantitative MR imaging of two-pool magnetization transfer model parameters in myelin mutant shaking PUP. NeuroImage. 2012; 62:1390–1398. [PubMed: 22664569]

Schmierer K, Scaravilli F, Altmann DR, Barker GJ, Miller DH. Magnetization transfer ratio and myelin in postmortem multiple sclerosis brain. Ann. Neurol. 2004; 56:407–415. [PubMed: 15349868]

Seifert AC, Wright AC, Wehrli SL, Ong HH, Li C, Wehrli FW. 31P NMR relaxation of cortical bone mineral at multiple magnetic field strengths and levels of demineralization. NMR Biomed. 2013; 26:1158–1166. [PubMed: 23505120]

Sheth V, Shao H, Chen J, Vandenberg S, Corey-Bloom J, Bydder GM, Du J. Magnetic resonance imaging of myelin using ultrashort Echo time (UTE) pulse sequences: Phantom, specimen, volunteer and multiple sclerosis patient studies. Neuroimage. 2016; 136:37–44. [PubMed: 27155128]

Sussman MS, Pauly JM, Wright GA. Design of practical T2-selective RF excitation (TELEX) pulses. Mag. Res. Med. 1998; 40:890–899.

van der Knaap, MS., Valk, J. Magnetic Resonance of Myelination and Myelin Disorders. Springer; Berlin ; New York: 2005. p. 1-19.

Vavasour IM, Laule C, Li DKB, Traboulsee AL, MacKay AL. Is the magnetization transfer ratio a marker for myelin in multiple sclerosis? J. Magn. Reson. Imaging. 2011; 33:713–718. [PubMed: 21563257]

Waldman A, Rees JH, Brock CS, Robson MD, Gatehouse PD, Bydder GM. MRI of the brain with ultra-short echo-time pulse sequences. Neuroradiology. 2003; 45:887–892. [PubMed: 14508620]

Wehrli FW, MacFall JR, Shutts D, Breger R, Herfkens RJ. Mechanisms of Contrast in NMR Imaging. JCAT. 1984; 8:369–380.

Weiger M, Brunner DO, Dietrich BE, Muller CF, Pruessmann KP. ZTE imaging in humans. Magn Reson Med. 2013; 70:328–332. [PubMed: 23776142]

Weiger M, Pruessmann K. MRI with Zero Echo Time. eMagRes. 2012; 1:311–322.

Weiger M, Wu M, Wurnig MC, Kenkel D, Boss A, Andreisek G, Pruessmann KP. ZTE imaging with long-T2 suppression. NMR Biomed. 2015; 28:247–254. [PubMed: 25521814]

Wennerstrom H. Proton nuclear magnetic resonance lineshapes in lamellar liquid crystals. Chem. Phys. Lett. 1973; 18:41–44.

Wessel D, Flügge UI. A method for the quantitative recovery of protein in dilute solution in the presence of detergents and lipids. Anal. Biochem. 1984; 138:141–143. [PubMed: 6731838]

Whittall K, Mackay A. Quantitative interpretation of NMR relaxation data. Mag. Res. Med. 1989; 84:134–152.

Whittall KP, MacKay AL, Graeb DA, Nugent RA, Li DK, Paty DW. In vivo measurement of T2 distributions and water contents in normal human brain. Magn Reson Med. 1997; 37:34–43. [PubMed: 8978630]

Wilhelm, MJ., Ong, HH., Wehrli, FW. Super-Lorentzian framework for investigation of T2* distribution in myelin. Proceedings of the 20th Annual ISMRM Scientific Meeting. ISMRM; Melbourne, Australia. 2012a. p. 2394

Wilhelm MJ, Ong HH, Wehrli SL, Li C, Tsai PH, Hackney DB, Wehrli FW. Direct magnetic resonance detection of myelin and prospects for quantitative imaging of myelin density. Proc Natl Acad Sci U S A. 2012b; 109:9605–9610. [PubMed: 22628562]

Wu Y, Chesler DA, Glimcher MJ, Garrido L, Wang J, Jiang HJ, Ackerman JL. Multinuclear solid-state three-dimensional MRI of bone and synthetic calcium phosphates. Proc. Natl. Acad. Sci. USA. 1999; 96:1574–1578. [PubMed: 9990066]

Zhang B, Lee JS, Khitrin A, Jerschow A. Long lived NMR signal in bone. J Magn Reson. 2013; 231:1–4. [PubMed: 23562664]

Highlights

9.4T spinal cord myelin density maps show expected contrast between GM and WM

IR-preparation suppression pulses effectively suppress long-T_2 signal in white matter

Myelin densities measured in white matter are in the range of 18.1% to 23.5%

Myelin density measurements are consistent in non-exchanged and D_2O-exchanged cords

Feasibility of direct myelin imaging with ZTE was shown on a 3T clinical scanner
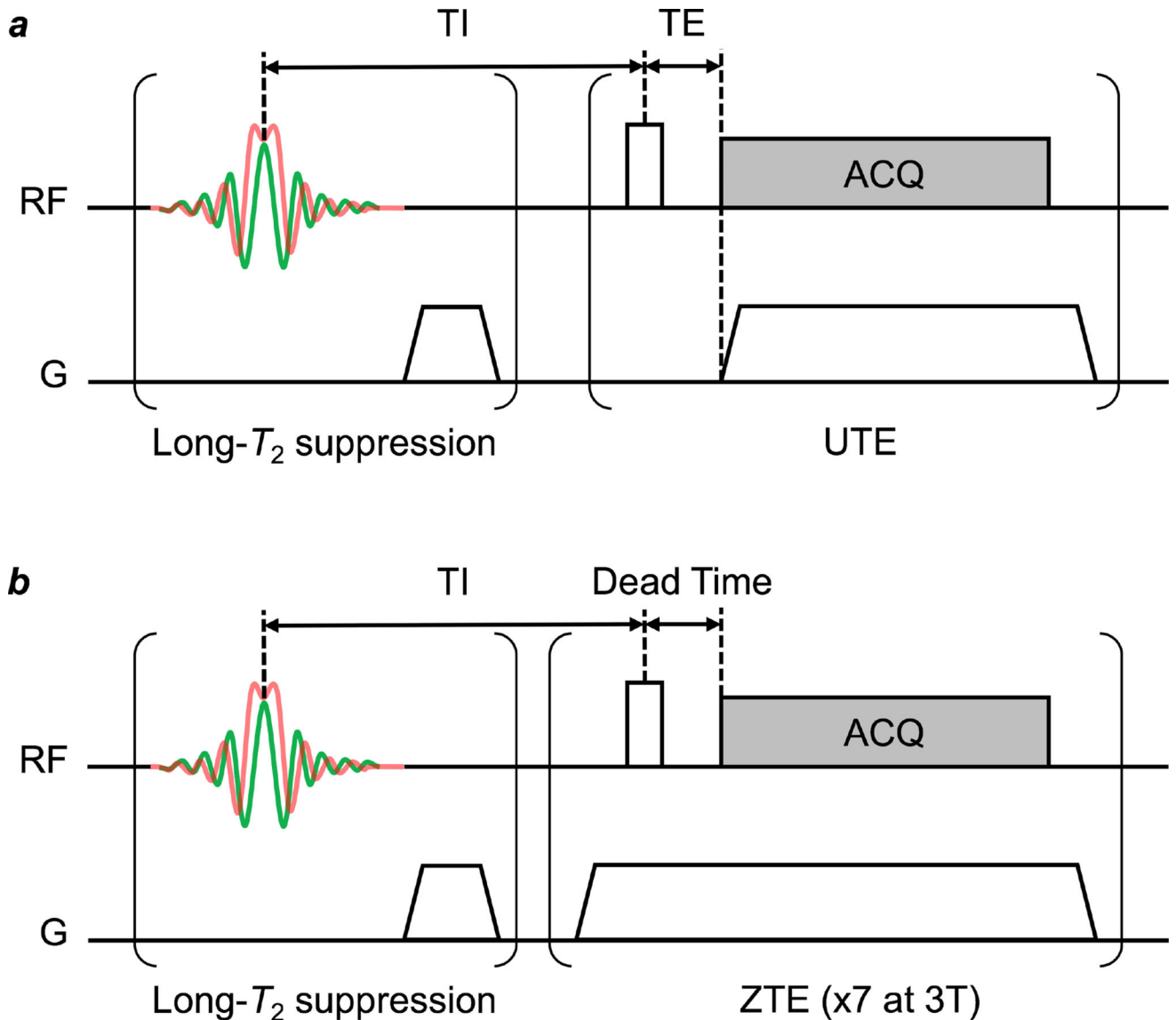
Figure 1.
Schematic diagram of UTE (a) and ZTE (b) pulse sequences. In UTE, an RF pulse followed by data acquisition (ACQ) simultaneously with the readout gradient ramp, while in ZTE the readout gradient is first ramped to full strength to allow eddy currents to dissipate before the RF pulse is applied. Adiabatic inversion recovery (IR)-based long-T_2 suppression, consisting of a hyperbolic secant (HS_1) pulse with bandwidth = 5 kHz and duration = 5 ms followed by a spoiler gradient and an inversion recovery delay (TI), selectively nulls non-myelin ^{1}H magnetization. Long-T_2 magnetization is inverted by the HS_1 pulse, while short-T_2 magnetization undergoes transverse relaxation during the pulse and is saturated rather than inverted. Both the inverted long-T_2 and saturated short-T_2 magnetization then undergo longitudinal relaxation, such that at time TI, the long-T_2 magnetization is nulled ($M_z = 0$) and the short-T_2 magnetization has recovered ($M_z > 0$). A UTE or ZTE imaging readout applied at this point will selectively image the short-T_2 ^{1}H signal arising from myelin matrix

protons. At 3T, seven ZTE readouts, at a repetition interval of 2 ms, are executed after each IR-based long-T_2 suppression module.
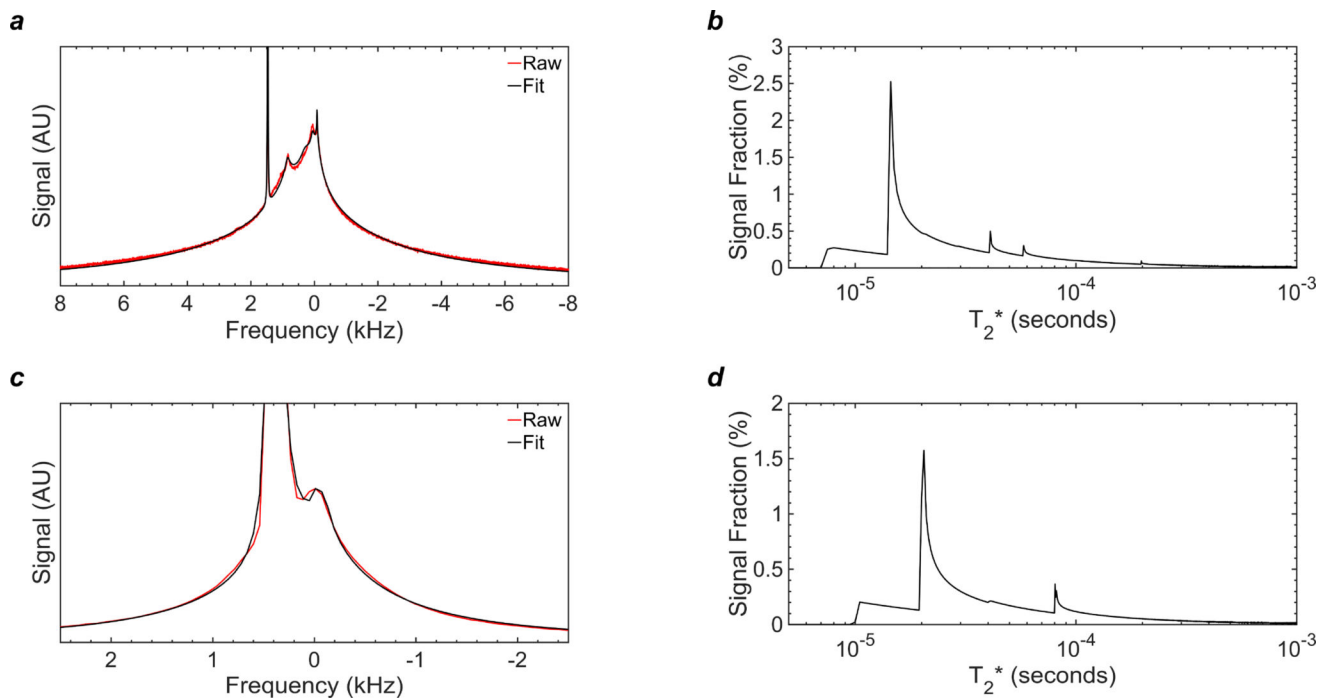
Figure 2.
^{1}H NMR spectra and T_2^* analysis of myelin signal at 37°C following D_2O exchange of tissue water: (a) NMR spectrum (red) collected at 9.4T and SL-based fit (black) of myelin extract derived from ovine cervical spinal cord; (b) T_2^* histogram of the myelin lipid components derived from SL fitting in panel (a); (c) NMR spectrum (red) collected at 3T and SL-based fit (black) of intact ovine cervical spinal cord; (d) T_2^* histogram of the myelin lipid components derived from the SL fitting in panel (c). The spectra both consist of a broad envelope with relatively narrow components centered at the methylene lipid frequency, consistent with a dipolar-broadened lamellar liquid crystal system.
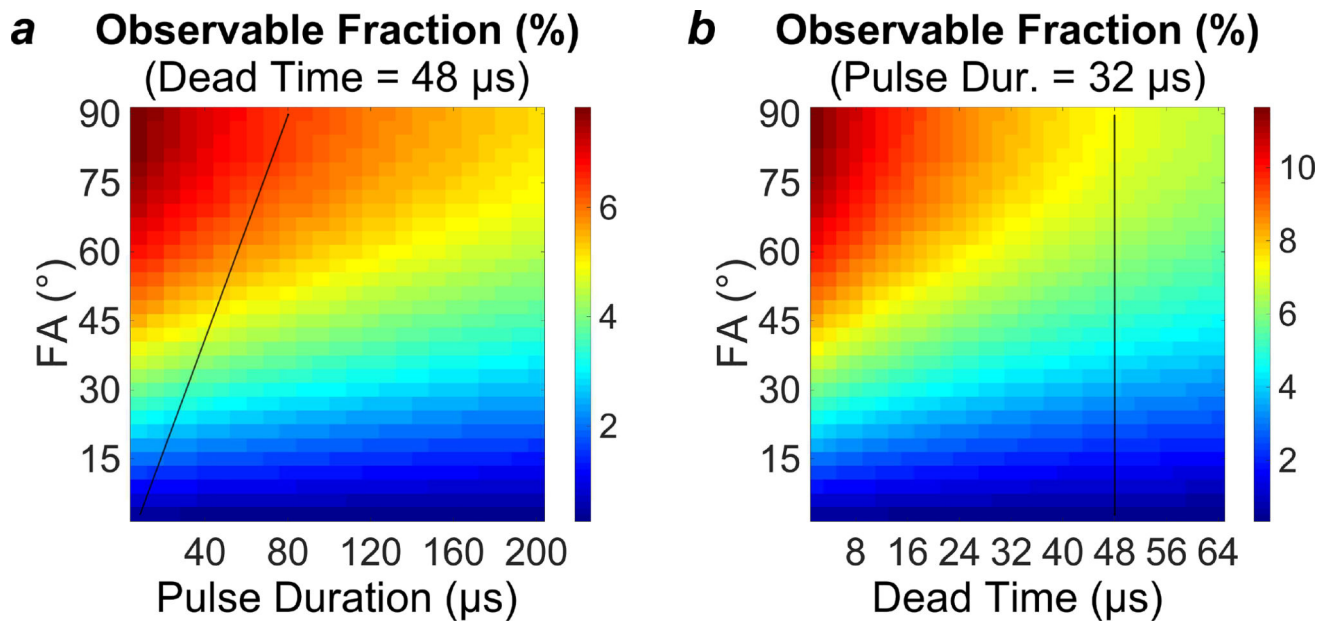
Figure 3.
Plots of the observable fraction of the total longitudinal magnetization. (a) Observable fraction as a function of flip angle (FA) and pulse duration (t_p), at a constant TE of 48 μs. (b) Observable fraction as a function of flip angle and TE, at constant pulse duration of 32 μs. Black lines superimposed on the plots illustrate the capabilities of the RF hardware used in the 3T imaging portion of this work.
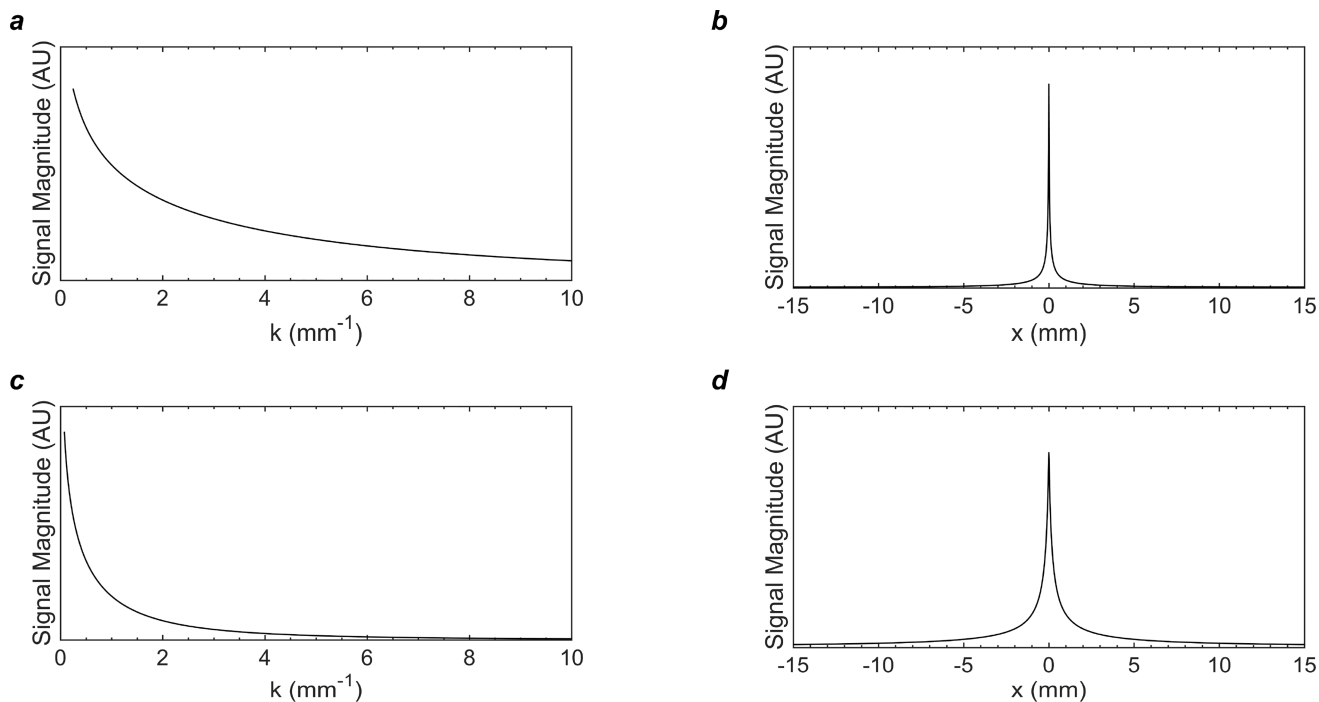
Figure 4.

Modulation transfer functions (MTFs, a, c) and point-spread functions (PSFs, b, d) of myelin ^{1}H signal at 9.4 T, assuming a 230.9 mT/m encoding gradient, and 3 T, assuming a 36.7 mT/m encoding gradient, based on the calculated T2* distributions shown in Fig. 2. The full width at half maximum (FWHM) of the PSF was 380 μm at 3 T, using a 36.7 mT/m encoding gradient, and 64 μm at 9.4 T, using a 230.9 mT/m encoding gradient. The FWHM is an imperfect criterion of intrinsic spatial resolution for a super-Lorentzian lineshape, which has a narrow central peak and broad, high tails.
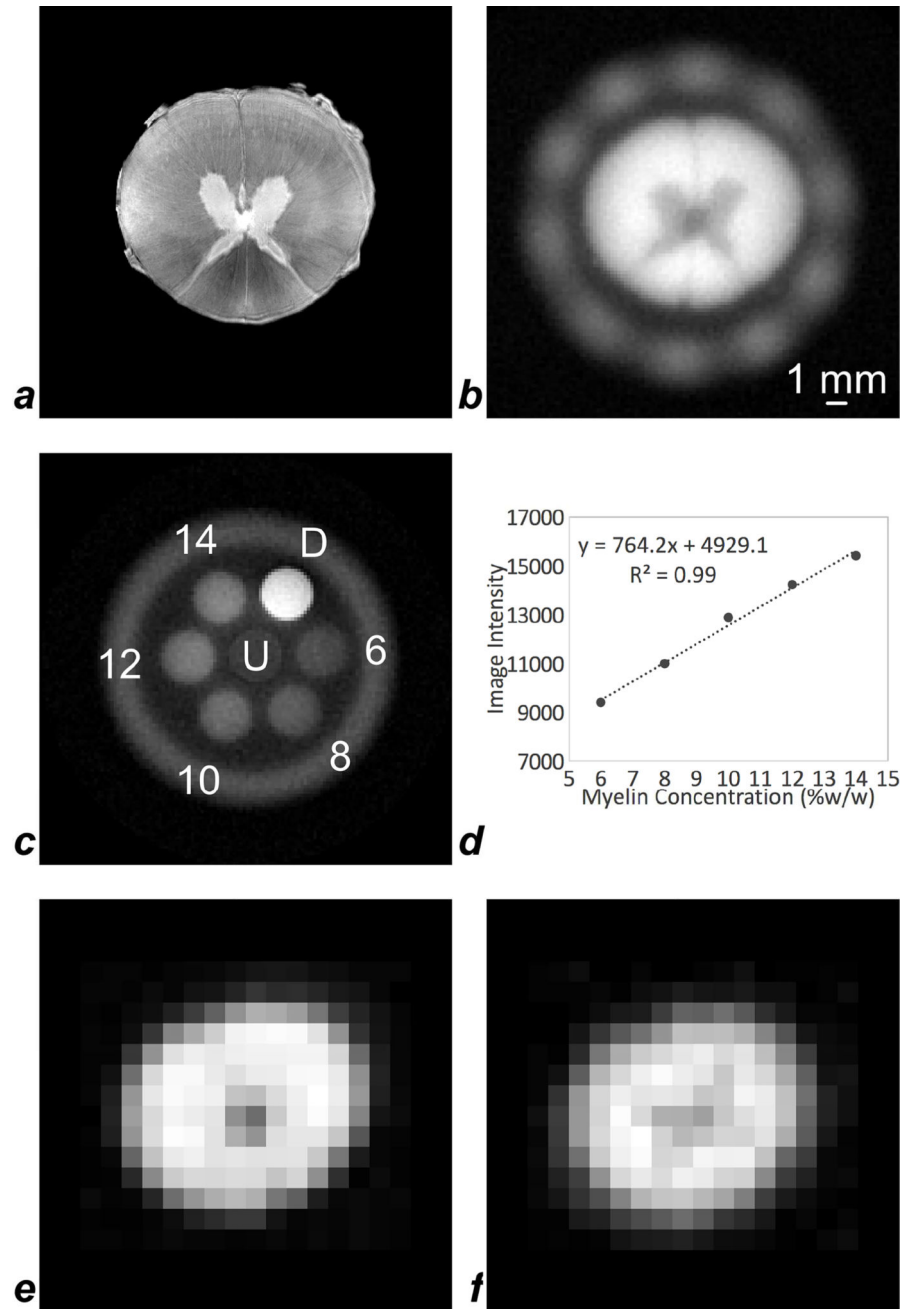
Figure 5.

A montage of representative images of spinal cord and myelin extract reference samples: (a) high-resolution 9.4T RARE image of the spinal cord, for visual reference (voxel size 51 μm × 51 μm × 400 μm); (b) 9.4T ZTE image of the D_2O-exchanged spinal cord in a 15-mm RF coil, in which signal intensity is higher in the myelin-rich white matter than in the gray matter (voxel size 188 μm × 188 μm × 375 μm). The plastic of the RF coil is visible as a hazy ring of signal surrounding the spinal cord. (c) 9.4T ZTE image of five concentrations of myelin extract in D_2O, along with un-doped, labeled 'U', and 14 mM $MnCl_2$-doped, labeled 'D', mixtures of 10% H_2O and 90% D_2O, in a 15-mm RF coil (voxel size 250 μm × 250 μm

× 625 μm); (d) signal intensities in the five myelin extract references are strongly correlated to their concentrations; (e) ZTE-PETRA and (f) IR-rZTE-PETRA images of the D_2O-exchanged spinal cord acquired on a 3T human scanner with a custom PTFE solenoid coil. Although image resolution is reduced due to lower gradient amplitude achievable at 3T (36.7 mT/m) compared to 9.4T (230.9 mT/m), the lower intensity of the central gray matter is apparent. For both (e) and (f) voxel size was 1 mm isotropic.
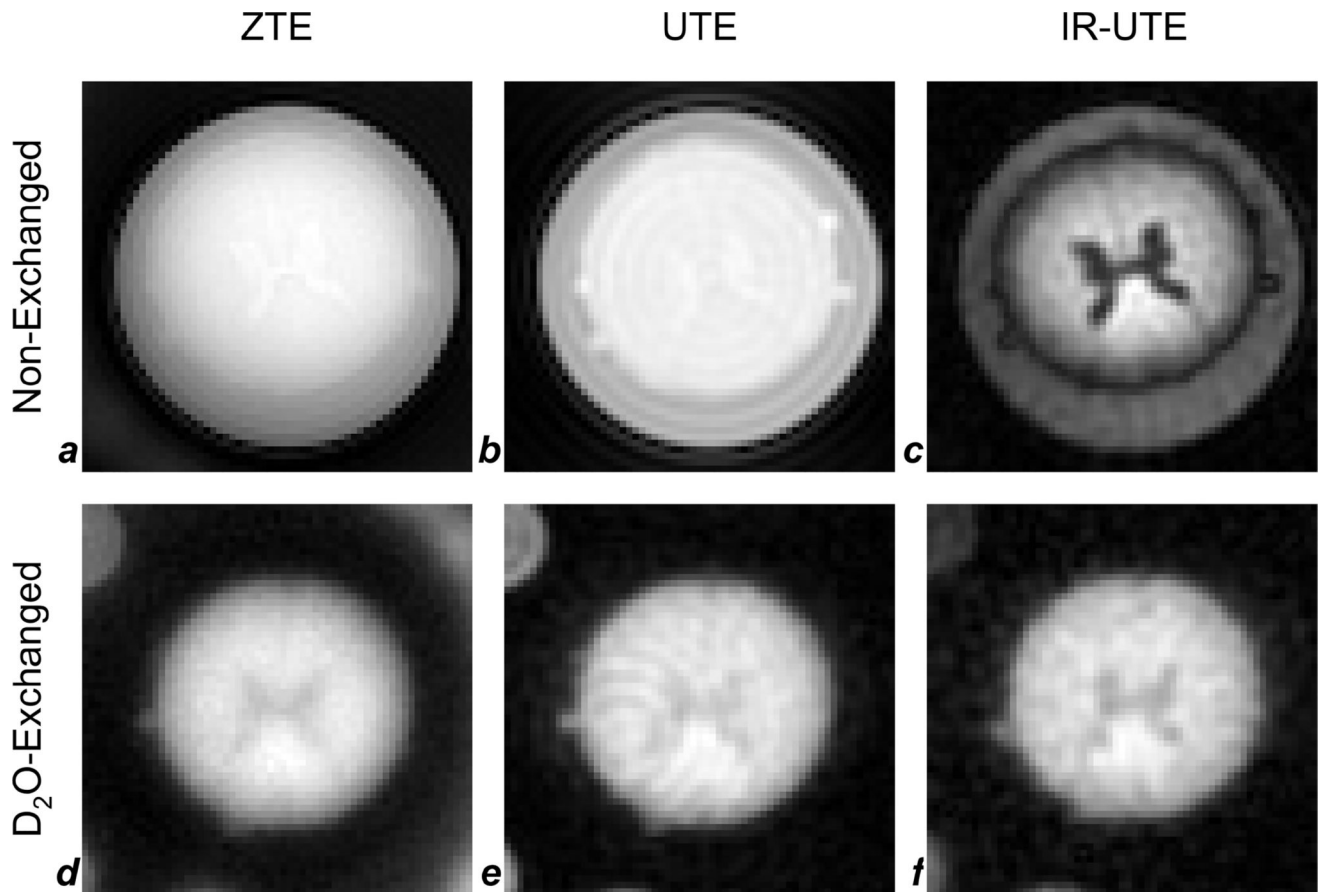
Figure 6.
9.4T images of spinal cord before (a–c) and after (d–f) D_2O-exchange. Images were acquired with ZTE (a,d), UTE (b,e), and IR-UTE (c,f) pulse sequences at 250 μm × 250 μm × 750 μm voxel size. In the non-exchanged cord without long-T_2 suppression (a,b), gray matter has slightly higher signal intensity than white matter, reflecting its greater ^{1}H density, while in the image with long-T_2 suppression (c), water in the gray matter is effectively suppressed, and white matter signal (arising predominantly from myelin) is preserved. Free water surrounding the spinal cord has longer T_1 than tissue water in the cord, causing it to be less fully suppressed at an inversion recovery time optimized for tissue water (TR = 200 ms and TI = 90 ms). In images of D_2O-exchanged samples (d–f), gray matter has lower signal intensity than white matter for all three sequences, due to the replacement of tissue water with D_2O. SNRs in nonexchanged ZTE (a), UTE (b), and IR-UTE (c) images were 23, 7.8, and 18, respectively, and SNRs in the D_2O-exchanged ZTE (d), UTE (e), and IR-UTE (f) images were 24, 20, and 19, respectively.
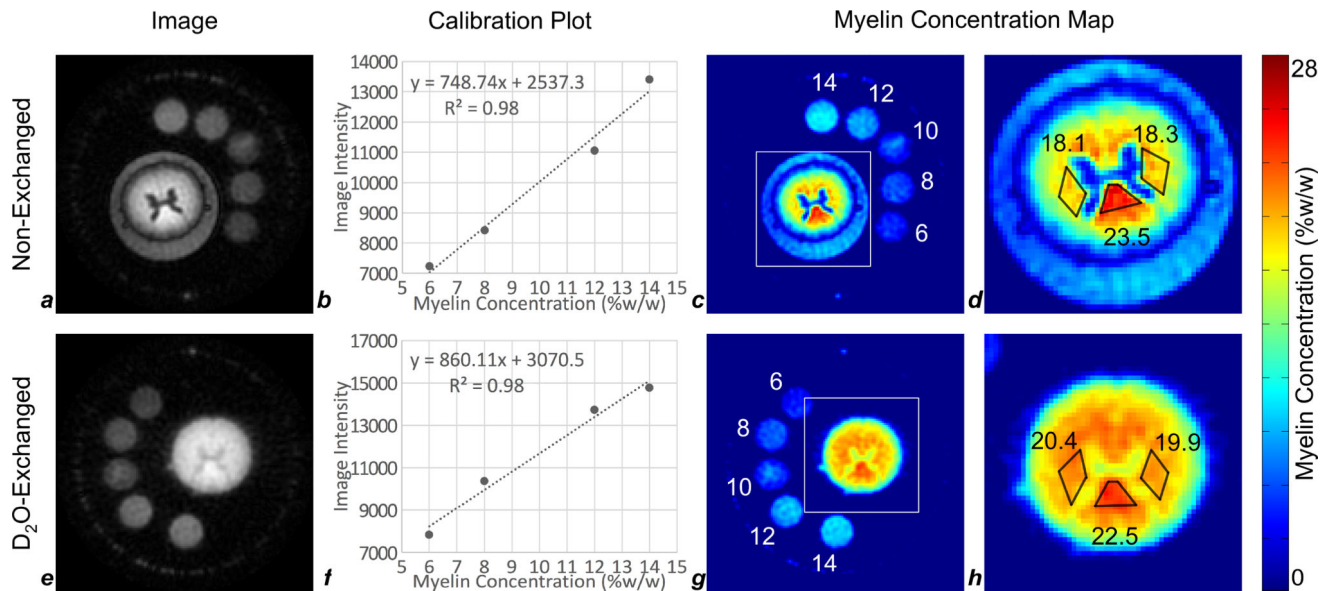
Figure 7.
Image-based quantification of myelin at 9.4T in ovine cervical spinal cords before (a–d) and after (e–h) deuterium exchange. Voxel size in all images is $250 \times 250 \times 750$ µm^3. Intensity within each reference sample (6%, 8%, 10%, 12%, and 14% myelin extract, by weight, in D_2O) quantified in the raw images (a,e), was used to generate standard curves (b,f). Image intensity is well-correlated to myelin extract concentration for 6%, 8%, 12%, and 14% references. Using the calibration curves (b,f), raw images were converted to maps of myelin density (c,g). Areas indicated by the white squares (c,g) are enlarged in (d,h). Myelin density was quantified in three white matter ROIs (left and right lateral fasciculi, and dorsal columns). The residual signal surrounding the spinal cord in (c,d) is due to incomplete suppression of free water surrounding the cord due to longer T_1 than tissue water within the spinal cord, therefore being incompletely suppressed at a TI chosen for optimal nulling of tissue water signal.